Inorganic Chemistry

Article

pubs.acs.org/IC

Charge-Coupled Substituted Garnets $(Y_{3-x}Ca_{0.5x}M_{0.5x})Fe_5O_{12}$ (M = Ce, Th): Structure and Stability as Crystalline Nuclear Waste Forms

Xiaofeng Guo,[†,‡,§] Ravi K. Kukkadapu,[∥] Antonio Lanzirotti,[⊥] Matthew Newville,[⊥] Mark H. Engelhard,[∥] Stephen R. Sutton,[⊥,#] and Alexandra Navrotsky*[,†]

[†]Peter A. Rock Thermochemistry Laboratory and Nanomaterials in the Environment, Agriculture and Technology Organized Research Unit and [§]Department of Chemistry, University of California, Davis, California 95616, United States

[‡]Earth and Environmental Sciences Division, Los Alamos National Laboratory, Los Alamos, New Mexico 87545, United States

[∥]Environmental Molecular Sciences Laboratory, Pacific Northwest Laboratory, Richland, Washington 99354, United States

[⊥]Center for Advanced Radiation Sources and [#]Department of Geophysical Sciences, University of Chicago, Chicago, Illinois 60637, United States

Supporting Information

ABSTRACT: The garnet structure has been proposed as a potential crystalline nuclear waste form for accommodation of actinide elements, especially uranium (U). In this study, yttrium iron garnet (YIG) as a model garnet host was studied for the incorporation of U analogs, cerium (Ce) and thorium (Th), incorporated by a charge-coupled substitution with calcium (Ca) for yttrium (Y) in YIG, namely, $2Y^{3+} = Ca^{2+} + M^{4+}$, where $M^{4+} = Ce^{4+}$ or Th^{4+}. Single-phase garnets $Y_{3-x}Ca_{0.5x}M_{0.5x}Fe_5O_{12}$ ($x = 0.1-0.7$) were synthesized by the citrate−nitrate combustion method. Ce was confirmed to be tetravalent by X-ray absorption spectroscopy and X-ray photoelectron spectroscopy. X-ray diffraction and ^{57}Fe−Mössbauer spectroscopy indicated that M^{4+} and Ca^{2+} cations are restricted to the *c* site, and the local environments of both the tetrahedral and the octahedral Fe^{3+} are systematically affected by the extent of substitution. The charge-coupled substitution has advantages in incorporating Ce/Th and in stabilizing the substituted phases compared to a single substitution strategy. Enthalpies of formation of garnets were obtained by high temperature oxide melt solution calorimetry, and the enthalpies of substitution of Ce and Th were determined. The thermodynamic analysis demonstrates that the substituted garnets are entropically rather than energetically stabilized. This suggests that such garnets may form and persist in repositories at high temperature but might decompose near room temperature.

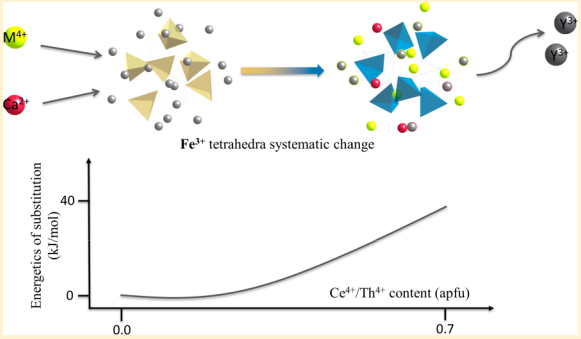

INTRODUCTION

Although borosilicate and phosphate glassy matrices are currently used as nuclear waste forms,[1−5] there is still potential need for more durable waste forms, such as crystalline ceramics, especially for actinides. A large body of research has been done on various tailored ceramic waste forms, such as monazite, pyrochlore, zircon, zirconolite, and defect fluorite.[5−18] Among such candidate mineral phases, garnet is a new storage form suggested for incorporation of actinides.[11,14,15,17,19−30] The long-term stability of garnet has been confirmed by the recent discovery of a natural uranium (U) containing garnet, elbrusite−(Zr).[19] Its significant U content, ∼27 wt % U, suggests garnet can be a good waste form for U. Garnets with higher concentrations of U, up to ∼about 30 wt %,[11,31] have been formed in laboratory studies.[10,11,19,21,22,26,31] The garnet structure has great chemical flexibility due to the presence of sites with 8-, 6-, and 4-fold coordination and the possibility of distortions and/or cation ordering to better accommodate substitutions of different elements derived from spent nuclear fuel or dismantled nuclear weapons. The radiation tolerance of garnet was studied extensively[20−22] and found to be comparable to that of other ceramic waste forms and only weakly related to its chemical composition, suggesting that it is topologically constrained and therefore relatively uniform for different compositions. Even though garnet becomes amorphous at low radiation dose[23] or becomes completely metamict as in elbrusite−(Zr),[19] its chemical stability is not heavily compromised due to the amorphization[23,24] and it performs well in leaching studies compared to other ceramic nuclear waste hosts.[16,24] Thus, one can tailor garnet composition without compromising radiation response and stability under incorporation of high levels of actinides.

Yttrium iron garnet, $Y_3Fe_5O_{12}$ (YIG), a simple iron garnet, was chosen as a host garnet in this study and in previous studies.[25−27] YIG has three different types of polyhedra in its

Received: February 25, 2015
Published: April 8, 2015

DOI: 10.1021/acs.inorgchem.5b00444
Inorg. Chem. 2015, 54, 4156−4166

three-dimensional framework[28−30] (Figure 1). YO_8 dodecahedral *c* sites are edge sharing with both FeO_6 octahedral *a* sites

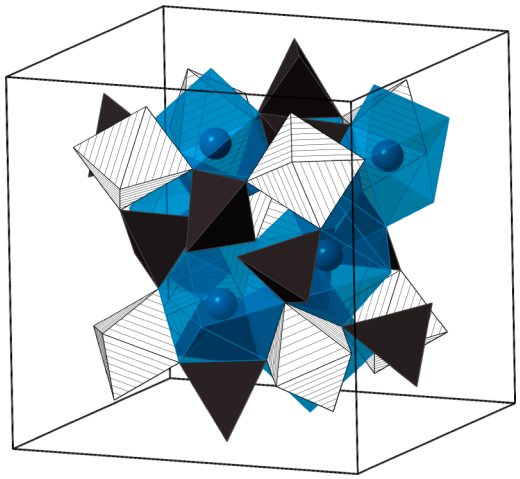

Figure 1. Schematic representation of garnet structure. Translucent blue polyhedra are *c* sites occupied by Y and Ce or Th. Octahedra (dashed) are *a* cites, and tetrahedra (black) are *d* cites.

and FeO_4 tetrahedral *d* sites, and the latter two polyhedra share corners alternately. Among these three polyhedral sites, the large 24*c* dodecahedral site accommodates large tetravalent ions, such as Ce, Th, and U.[25,27,29,31,32]

The complicated uranium substitution in garnet is a challenge for determining structural and energetic changes. Common oxidation states of U in garnet are tetravalent and hexavalent and correlate with different U site occupancies. Such complications have created difficulties in determining the crystal chemical formula for some synthetic garnet systems[21] whose compositions are close to elbrusite−(Zr) and for other ferrigarnet systems.[11,33] First-principles calculations also show the complexity of U incorporation in $Ca_3(Ti,Zr,Hf,Sn)_2(Fe_2Si)O_{12}$ garnet matrices[34] and in YIG garnet.[35] Thus, the structural and energetic effects of Ce and Th incorporation in YIG were studied previously as a simpler model system.[26,27] In Ce-substituted YIG, $Y_{3-x}Ce_xFe_5O_{12}$ (Ce:YIG), Ce was found to exist in different oxidation states. At low Ce content, there is some Ce^{3+} present. With increasing Ce content, cerium exists mostly as Ce^{4+} in dodecahedral sites coupled with reduced Fe^{2+} in tetrahedral sites.[26] Th is tetravalent; thus, tetrahedral Fe^{3+} is reduced in order to compensate for the extra charge introduced by Th^{4+} substituting for Y^{3+} to form $Y_{3-x}Th_xFe_5O_{12}$.[27] Energetics of both these substitutions, in low concentration, have a near neutral effect, due to the competition between energetically favorable lattice relaxation that attenuates strain energy and energetically unfavorable reduction effects.[26] This competition also hinders further substitution of Ce or Th ions in YIG.[27]

Thus, to minimize the destabilizing contribution from iron reduction and enhance the stability of substituted garnet phase, charge-coupled Ca^{2+}−M^{4+} substitution is proposed as a new substitution strategy to incorporate large tetravalent cations in YIG. Here Ca^{2+} is introduced as a divalent cation to balance the extra charge from the substitution of M^{4+} for Y^{3+}. Other divalent cations, such as Mg^{2+}, can also be considered in this strategy. Although magnesium is abundant in natural garnet minerals, it is smaller in size than calcium, which increases the size difference between the divalent ion and the lanthanide or actinide and may make Mg-rich garnets less suitable for actinide incorporation. Previously, Ca^{2+}−Ln^{4+} (Ln = Ce, Pr, Tb) charge-coupled substituted garnet compounds with large Ln loads were synthesized.[36] A large loading of Ce or Th in YIG following this substitution scheme is expected to occur. In this study, $Y_{3-x}Ca_{0.5x}M_{0.5x}Fe_5O_{12}$ (M = Ce, Th) garnets with up to $0.5x$ = 0.7 atoms per formula unit (apfu) of Ce or Th were synthesized. With increasing substitution, the structural change was traced by distortions of Fe in octahedral and tetrahedral sites by using ^{57}Fe−Mössbauer spectroscopy. X-ray absorption near-edge structure spectroscopy (XANES) and X-ray photoelectron spectroscopy (XPS) were performed to evaluate cerium oxidation state.

Enthalpies of formation and enthalpies of substitution were obtained by high temperature oxide melt solution calorimetry. By analyzing the structure and thermodynamics of both series of garnet samples, we studied the effect of Ca^{2+}, M^{4+} cation substitution on the stability of these charge-coupled substituted YIGs. These results were analyzed to provide insights into waste form development.

EXPERIMENTAL METHODS

Reagents, $Ca(NO_3)_3{\cdot}4H_2O$ (Fisher, 99%), $Fe(NO_3)_3{\cdot}9H_2O$ (Sigma-Aldrich, 99.99%), and $(NH_4)_2Ce(NO_3)_6$ (Alfa Aesar, 99%) or $Th(NO_3)_4{\cdot}5H_2O$ (CERAC, 99%), were mixed in appropriate stoichiometry and dissolved in deionized water. An aqueous solution of citric acid monohydrate (Alfa Aesar, 99.9%) was added, and the ratio of citric acid to nitrate was kept at about 0.75.[37] This solution was heated at ∼90 °C while being constantly stirred by a magnetic bar to ensure homogeneity, until viscous gels formed. The gels were then heated to 350 °C in about 2 h for drying. The dried powder was heated at 700 °C for 0.5 h for reaction through self-propagating combustion[38] to form aggregates of loose powders, which were then pelletized for further calcination in air at 1300 °C for 24 h. $Y_{3-x}Ca_{0.5x}M_{0.5x}Fe_5O_{12}$ (M = Ce, Th) samples are denoted by $0.5x$Ca,$0.5x$M:YIG, where the coefficient $0.5x$ represents the concentration of Ce or Th in a nominal composition of $Y_{3-x}Ca_{0.5x}M_{0.5x}Fe_5O_{12}$.

X-ray powder diffraction (XRD) measurements were performed with a Bruker D8 diffractometer (Cu Kα radiation, 40 kV, 30 mA). XRD patterns were obtained in the range of 2θ = 16−80° with a step size of 0.016° with an exposure time of 1s step^{-1}. Elemental analysis was conducted using a Cameca SX-100 electron microprobe with wavelength-dispersive spectroscopy (15 kV accelerating voltage, 10 nA beam current and a spot size of 1 μm). The obtained powder samples were pelletized, sintered, and then polished prior to analysis. $Y_3Al_5O_{12}$, $CaWO_4$, Fe_2O_3, CeO_2, and ThO_2 were used as analytical standards. At least 10 measurements were done for each sample. Homogeneity was evaluated from X-ray mapping and electron backscatter imaging.

Mössbauer spectra were collected using either a WissEl Elektronik (Germany) or Web Research Co. (St. Paul, MN) instrument that included a closed-cycle cryostat SHI-850 obtained from Janis Research Co., Inc. (Wilmington, MA), a Sumitomo CKW-210 He compressor unit, and an Ar−Kr proportional counter detector with WissEl setup or a Ritverc (St. Petersburg, Russia) NaI detection system. A ^{57}Co/Rh source (50−75 mCi, initial strength) was used as the gamma energy source. With the WissEl setup, the transmitted counts were stored in a multichannel scalar as a function of energy (transducer velocity) using a 1024-channel analyzer. In both setups (WissEl and Web Research Co.) the raw data were folded to 512 channels to provide a flat background and a zero-velocity position corresponding to the center shift (CS) of a metal alpha-Fe foil at room temperature. Calibration spectra were obtained with a 25 μm thick Fe foil (Amersham, England) placed in the same position as the samples to minimize any geometry errors. The Mössbauer data were modeled with Recoil software using a Voigt-based structural fitting routine.[39] Sample preparation is identical to the previously reported procedures.[40]

DOI: 10.1021/acs.inorgchem.5b00444
Inorg. Chem. 2015, 54, 4156−4166

XANES spectroscopy was performed at the GSECARS X-ray microprobe beamline (13-ID-E) at the Advanced Photon Source (APS), Argonne National Laboratory (Argonne, IL, USA). Detailed information on procedures can be found in the literature.[41] Cerium XANES spectra were collected in fluorescence mode with a 4-element, silicon-drift-diode, solid-state, X-ray fluorescence detector (Vortex-ME4, Hitachi High-Technologies Science America, Inc.). Fluorescence XANES spectra were corrected for detector dead time and for self-absorption based on the calculated chemical formulas for each compound and using the algorithm published by Haskel.[42] XANES spectra of Ce(IV)O_2 and Ce(III)PO_4 standards were measured in transmission mode with He-(I_0) and N_2-(I_1) filled ion chambers. XANES spectra were obtained by scanning the monochromator through the Ce LIII absorption edge (~5725 eV) and recording both the Ce L_α fluorescence and the total absorption. The energy step sizes were 5 eV from 5623 to 5713 eV, 0.25 eV from 5713 to 5748 eV, and 1.0 eV from 5748 to 6100 eV. Dwell time at each energy step was 2 s, and up to nine spectra were collected and summed to improve the signal-to-noise. Energy calibration was obtained using an Fe metal foil (first derivative peak) and measured to be 7111.20 eV, consistent within uncertainty with the value reported by Kraft et al.[43] of 7111.29 eV. Samples and standards were prepared as thin powder layers mounted between Scotch tape. The X-ray absorption spectroscopy data processing software Athena[44] was used for analysis.

X-ray photoelectron spectroscopy (XPS) on garnet samples was performed using a Kratos Axis DLD spectrometer equipped with a monochromatic X-ray source of Al Kα (15 mA, 14 kV). The instrument work function was calibrated to give a binding energy (BE) of 83.96 ± 0.05 eV for the Au $4f_{7/2}$ line for metallic gold, and the spectrometer dispersion was adjusted to give a BE of 932.62 ± 0.05 eV for the Cu $2p_{3/2}$ line of metallic copper. High-resolution analyses were carried out with an analysis area of 300 × 700 μm and a pass energy of 80 eV. The Kratos charge neutralizer system was used on all specimens. Spectra have been charge corrected to the main line of the carbon 1s spectrum (adventitious carbon) set to 285.0 eV. Spectra were analyzed using CasaXPS software (version 2.3.16 PR 1.6).

A custom-built Tian-Calvet twin microcalorimeter[45,46] operated at 702 °C was used for measurements of enthalpies of drop solution (ΔH_{ds}) in molten sodium molybdate ($3NaO{\cdot}4MoO_3$) solvent. The chamber of the calorimeter was flushed with oxygen at ~50 mL/min to maintain a constant composition for the head space gas above the solvent. Oxygen was also bubbled through the melt at ~5 mL/min to maintain an oxidizing environment and to stir the solvent to facilitate dissolution of samples and prevent local saturation.[47] The calorimeter was calibrated by transposed temperature drops of ~5 mg α-Al_2O_3 pellets. For each experiment, the garnet sample was hand pressed as a ~5 mg pellet and weighed on a microbalance. Accuracy of the measurement was optimized by making multiple drops (5–10 per composition) of each sample. Uncertainties are reported as two standard deviations of the mean. The equipment, calibration, and experimental method have been described in detail elsewhere.[45,46,48]

RESULTS

The XRD patterns of Ca,Ce:YIGs and Ca,Th:YIGs are presented in Figure S1, Supporting Information. Single-phase garnets were obtained for Ce or Th content less than 0.7 apfu (x = 1.4). The phase purity of samples was confirmed by XRD and Mössbauer spectroscopy. The homogeneity of all samples was confirmed by electron backscatter imaging and X-ray mapping. The actual chemical compositions of garnet samples were acquired from electron microprobe analysis and are shown in Tables S1 and S2, Supporting Information, for Ca,Ce:YIGs and Ca,Th:YIGs, respectively.

Lattice parameters were obtained by using a whole profile-fitting procedure, and Vegard's law was followed in that an approximately linear expansion of the lattice parameters was observed with increasing Ce or Th content (Figure 2). Lattice parameters r_{Ce} of Ca,Ce:YIG were related to the content of Ce

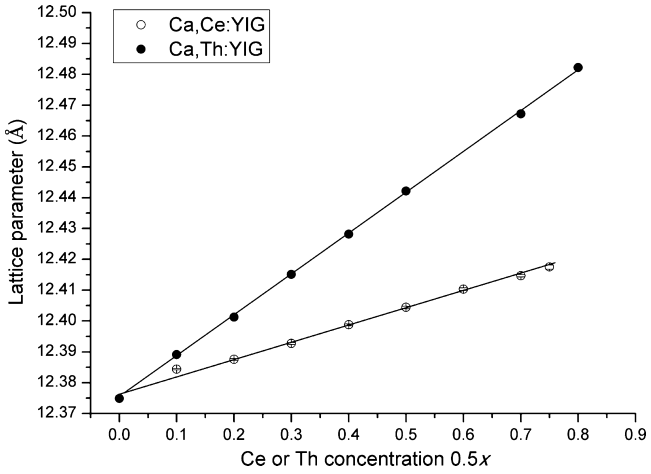

Figure 2. Lattice parameters of substituted garnets obtained from the whole profile fitting procedure against Ce concentration for Ca,Ce:YIGs (open circles) and against Th concentration for Ca,Th:YIGs (filled circles), which increase linearly with the Ce or Th concentration (adjusted R^2 for Ca,Ce:YIGs and Ca,Th:YIGs are 0.994 and 1.000, respectively).

in Ca,Ce:YIG by r_{Ce} = 12.378(1) + 0.051(2)·0.5x (Å), with adjusted R^2 = 0.994, and that of r_{Th} in Ca,Th:YIG is r_{Th} = 12.375(1) + 0.134(1)·0.5x (Å), with adjusted R^2 = 1.000. As expected, r_{Th} increases faster than r_{Ce}, because of the larger size of Th^{4+} than that of Ce^{4+}. For the maximum substitution amount, the lattice expands by 0.3% for Ca,Ce:YIG and 0.9% for Ca,Th:YIG.

Mössbauer spectroscopic data indicated that the samples are phase pure, without any contribution from either $YFeO_3$ or poorly crystalline/amorphous iron oxides, in agreement with XRD. The data also indicated that in all samples the octahedral:tetrahedral Fe^{3+} ratio is close to 2:3 (as in pure YIG), based on octahedral (a + a') and tetrahedral (d + d') Fe^{3+} sextet spectral areas (Tables 1 and S3, Supporting Information); only room-temperature-modeled spectra of $Y_{3-x}Ca_{0.5x}M_{0.5x}Fe_5O_{12}$ with 0.5x = 0.1 and 0.7 are shown in Figure 3. More importantly, the octahedral:tetrahedral Fe^{3+} ratio suggests that M^{4+} and Ca^{2+} cations are located mainly or entirely in dodecahedral sites. Spectra of Ca,Ce:YIGs are shown in Figure 4a, and those of Ca,Th:YIGs are shown in Figure 4b. Model-derived parameters are shown in Tables 1 and S3, Supporting Information.

Ce L_{III}-edge XANES spectra were collected on two cerium standards for comparison to Ca,Ce:YIG powders (Figure 5a). $CePO_4$ was analyzed as a representative trivalent Ce standard and CeO_2 as a representative tetravalent phase. The Ce L_{III} spectra for $CePO_4$ give an absorption edge energy (E_0) of 5724.4 eV and, as is true for other Ce^{3+} compounds, is characterized by the presence of a strong peak at about 5726.4 eV attributed to the dipole-allowed transition of Ce $2p_{3/2}$ to $4f^15d$ final states.[49] The tetravalent CeO_2 standard gives a higher E_0 value of ~5725.8. CeO_2 also shows, as other tetravalent Ce species do, a distinct spectral doublet at higher energy (with maxima at about 5730.3 and 5737.5 eV) of roughly equal intensity attributed to the presence of a mixture of the two cerium ground-state electronic configurations $4f^0$ and $4f^{15}\underline{0}$. CeO_2 spectra also typically display a small pre-edge structure generally considered a result of the dipole-forbidden $2p_{3/2}$ to 4f transition[50] and a low-energy shoulder due to

DOI: 10.1021/acs.inorgchem.5b00444
Inorg. Chem. 2015, 54, 4156–4166

Table 1. Modeled Room-Temperature Mössbauer Spectral Parameters of $Y_{3-x}Ca_{0.5x}Ce_{0.5x}Fe_5O_{12}$

sample x	sextet	HWHM,[a] mm/s	⟨CS⟩,[b] mm/s	⟨ε⟩,[c] mm/s	⟨|H|⟩,[d] mm/s	line width,[e] mm/s	%[f]
0 (YIG)[26]	Oct_a	0.132	0.37	0.06	49.0	0.45	28.7
	$Oct_{a'}$		0.37	−0.16	48.4	0.31	9.2
	Tet_d		0.06	0.08	40.2	0.55	20.6
	$Tet_{d'}$		0.18	−0.03	39.2	1.34	38.6
	Dodec		0.26	−0.10	50.2	1.87	2.9
0.1 ($Y_{2.9}Ce_{0.1}Fe_5O_{12}$)[26]	Oct_a	0.125	0.36	0.06	49.1	0.44	30.4
	$Oct_{a'}$		0.36	−0.17	48.4	0.30	9.5
	Tet_d		0.06	0.08	40.3	0.40	18.0
	$Tet_{d'}$		0.18	−0.03	39.3	1.05	42.1
0.2 (0.1Ca,0.1Ce:YIG)	Oct_a	0.135	0.37	0.06	49.0	0.48	28.5
	$Oct_{a'}$		0.39	−0.15	48.3	0.30	8.6
	Tet_d		0.05	0.10	40.1	0.57	18.1
	$Tet_{d'}$		0.19	−0.03	39.2	1.28	41.8
	Dodec		0.26	−0.10	48.5	1.00	3.1
0.2 ($Y_{2.8}Ce_{0.2}Fe_5O_{12}$)[26]	Oct_a	0.140	0.36	0.05	48.4	0.80	30.9
	$Oct_{a'}$		0.36	−0.17	47.7	0.32	8.8
	Tet_d		0.07	0.08	39.9	0.56	18.5
	$Tet_{d'}$		0.19	−0.03	39.2	1.05	30.8
	$Tet_{d''}$		0.11	−0.01	36.2	2.24	11.0
0.4 (0.2Ca,0.2Ce:YIG)	Oct_a	0.140	0.38	0.06	49.0	0.44	28.6
	$Oct_{a'}$		0.39	−0.15	48.4	0.22	7.6
	Tet_d		0.08	0.08	40.0	0.74	23.3
	$Tet_{d'}$		0.19	−0.04	39.2	1.40	36.6
	Dodec		0.20	−0.10	48.5	1.00	4.0
0.6 (0.3Ca,0.3Ce:YIG)	Oct_a	0.149	0.38	0.06	49.0	0.48	28.8
	$Oct_{a'}$		0.39	−0.14	48.3	0.29	8.1
	Tet_d		0.06	0.10	40.1	0.77	19.0
	$Tet_{d'}$		0.19	−0.04	39.2	1.59	40.8
	Dodec		0.25	−0.10	48.5	1.00	3.3
0.8 (0.4Ca,0.4Ce:YIG)	Oct_a	0.147	0.38	0.06	49.0	0.52	28.4
	$Oct_{a'}$		0.40	−0.14	48.3	0.32	8.1
	Tet_d		0.06	0.11	40.1	0.87	18.7
	$Tet_{d'}$		0.19	−0.04	39.2	1.67	41.2
	Dodec		0.25	−0.10	48.5	1.00	3.6
1.0 (0.5Ca,0.5Ce:YIG)	Oct_a	0.147	0.38	0.05	49.0	0.57	28.9
	$Oct_{a'}$		0.40	−0.15	48.2	0.30	7.4
	Tet_d		0.06	0.11	40.1	0.90	18.1
	$Tet_{d'}$		0.19	−0.04	39.1	1.74	42.0
	Dodec		0.25	−0.10	48.5	1.00	3.6
1.2 (0.6Ca,0.6Ce:YIG)	Oct_a	0.144	0.38	0.06	48.9	0.63	29.4
	$Oct_{a'}$		0.41	−0.15	48.2	0.35	7.8
	Tet_d		0.06	0.12	40.1	0.98	16.6
	$Tet_{d'}$		0.19	−0.04	39.1	1.77	42.8
	Dodec		0.25	−0.10	48.5	1.00	3.3
1.4 (0.7Ca,0.7Ce:YIG)	Oct_a	0.146	0.38	0.06	48.9	0.65	28.4
	$Oct_{a'}$		0.40	−0.14	48.2	0.34	7.7
	Tet_d		0.06	0.13	40.1	1.12	16.9
	$Tet_{d'}$		0.19	−0.05	39.1	1.91	43.1
	Dodec		0.25	−0.10	48.3	1.00	3.8

[a]Lorentzian half-width at maximum. [b]Center shift. [c]Quadrupole shift parameter. [d]Average hyperfine magnetic field. [e]Standard deviation or line width of H. [f]Relative % contribution (assuming identical recoilless fraction for the species).

splitting of the Ce 5d states in the cubic crystal field of the oxygen.

All measured Ca,Ce:YIG spectra, regardless of Ce content, give E_0 values of ~5725.8 eV within uncertainty, indistinguishable from E_0 measured for CeO_2 (Figure 5b). All Ca,Ce:YIG spectra display white line doublets considered indicative of tetravalent Ce. Linear component fitting of measured spectra with mixtures of spectra measured for $CePO_4$ and CeO_2 show that spectra are well modeled as solely CeO_2-like materials. In other words, within our ability to distinguish an additional spectral component at 5726.4 eV that may represent Ce^{3+}, these materials appear to contain no measurable trivalent Ce within error (as compared to the standard CeO_2). Small differences in the intensity of the white line doublets are observable relative to the edge step between samples, but we believe these differences most likely are due to the accuracy

DOI: 10.1021/acs.inorgchem.5b00444
Inorg. Chem. 2015, 54, 4156−4166

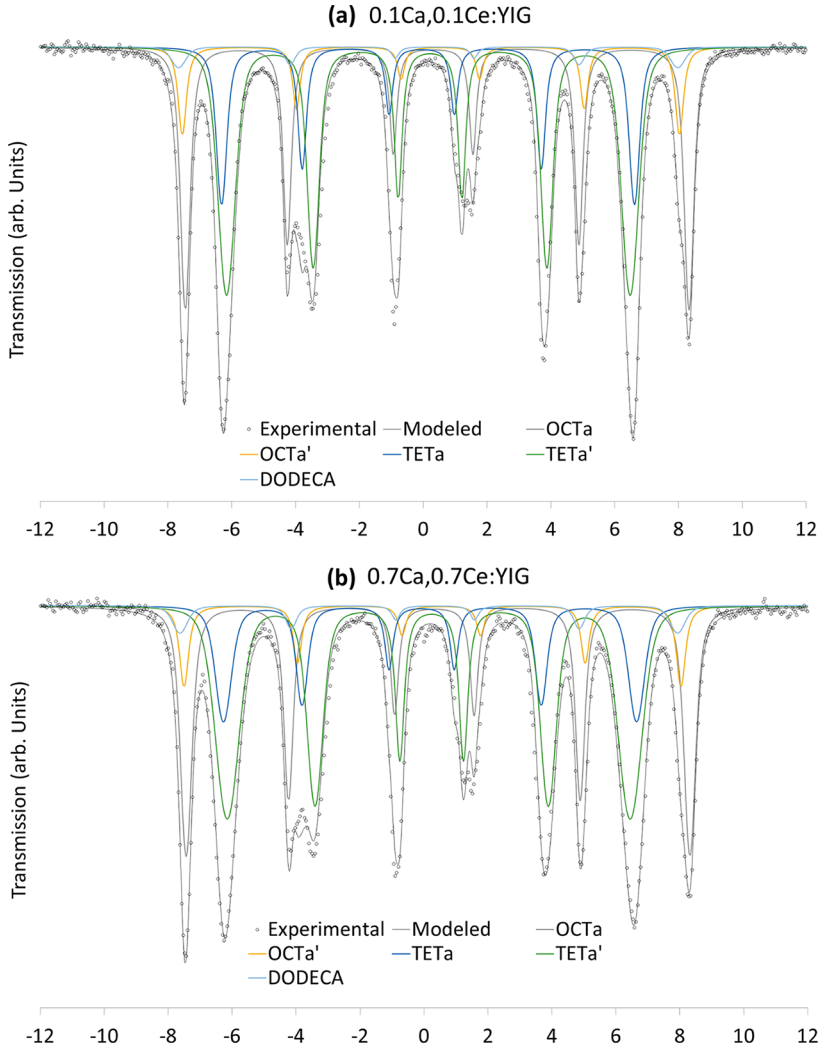

Figure 3. Mössbauer spectra modeled with two octahedral sextets (a and a′) and two tetrahedral sextets (d, d″) of Ca,Ce:YIG samples with $x = 0.2$ (a) and 1.4 (b).

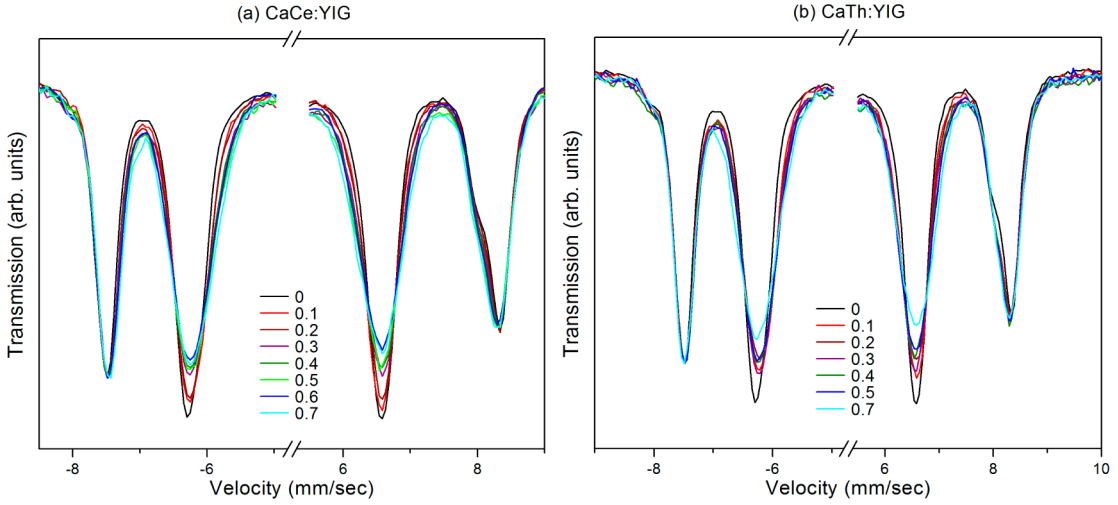

Figure 4. (a) Mössbauer spectra (from −8.5 to −5.5 and 5.5 to 8.5 mm/s regions) of Ca,Ce:YIG samples show broadening of (*a*, *a*′, *d*, and *d*′) sextets. (b) Mössbauer spectra (from −8.5 to −5.5 and 5.5 to 8.5 mm/s regions) of Ca,Th:YIG samples show broadening of (*a*, *a*‘, *d*, and *d*′) sextets.

with which the self-absorption correction can be applied. Even considering these intensity variations, no measurable Ce^{3+} can be identified.

XPS was performed on 0.7Ca,0.7Ce:YIG with the maximum Ce concentration. The Ce 3d spectral region is comprised of many peaks including the Ce $3d_{5/2}$ and Ce $3d_{3/2}$ lines at 882

DOI: 10.1021/acs.inorgchem.5b00444
Inorg. Chem. 2015, 54, 4156−4166

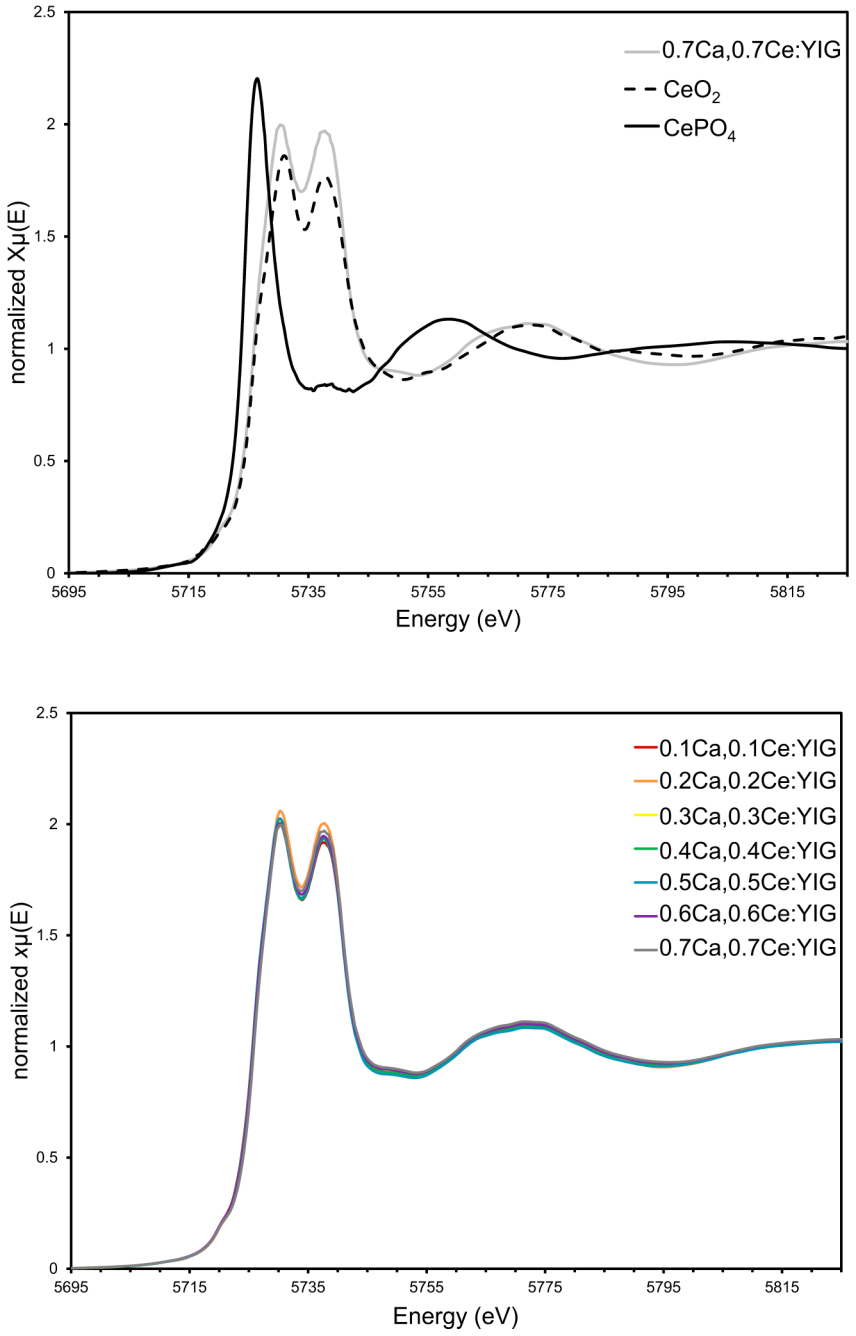

Figure 5. Cerium L_{III} XANES spectra for the 0.7Ca,0.7Ce:YIG and two standards: $Ce(IV)O_2$ and $Ce(III)PO_4$. $Ce(III)PO_4$ is characterized by a dominant peak at around 5727 eV, yet $Ce(IV)O_2$ has a doublet at higher energy range (about 5730−5738 eV) (top); cerium L_{III} XANES spectra for the 0.5*x*Ca,0.5*x*Ce:YIGs. All spectra are dominated by Ce^{4+} as indicated by the strong doublet at around 5730−5738 eV (bottom).

and 898 eV, respectively. In addition to the Ce 3d lines this spectral region has overlapping Fe Auger lines that extend from ~888.0 to 910.0 eV. The Ce $3d_{5/2}$ $4f^0$ line at 916.8 eV (Figure 6) confirms the presence of significant Ce^{4+} since this line is consistent with Ce^{4+} reference spectra.[51]

Enthalpies of drop solution (ΔH_{ds}, Table 2) of all garnet samples were directly obtained from high temperature oxide melt calorimetry. The reaction for dissolving each garnet sample is reaction 1 or 2 in Table 3. These values, along with known ΔH_{ds} values of Y_2O_3, CaO, Fe_2O_3, CeO_2, and ThO_2, were used to calculate the enthalpy of formation ($\Delta H_{f,ox}$, Table 2) of each garnet sample from binary oxides at room temperature. For Ca,Ce:YIG samples, thermochemical cycles (Table 3) were applied to derive their $\Delta H_{f,ox}$ from Y_2O_3, CaO, Fe_2O_3, and CeO_2. Similar thermochemical cycles (Table 3) were used to calculate $\Delta H_{f,ox}$ of Ca,Th:YIG from Y_2O_3, CaO, Fe_2O_3, and ThO_2. In addition, standard enthalpies of formation (ΔH^o_f, Table 2) of Ca,Ce:YIGs and Ca,Th:YIGs from elements were calculated based on thermochemical cycles in Table S4, Supporting Information.

DISCUSSION

Pure YIG (without any *c*-site Fe^{3+}) displays one tetrahedral and two octahedral sextets in its room-temperature Mössbauer spectrum.[57] This is due to the orientation of the electric field gradient of Fe^{3+} along one and two directions with respect to

DOI: 10.1021/acs.inorgchem.5b00444
Inorg. Chem. 2015, 54, 4156−4166

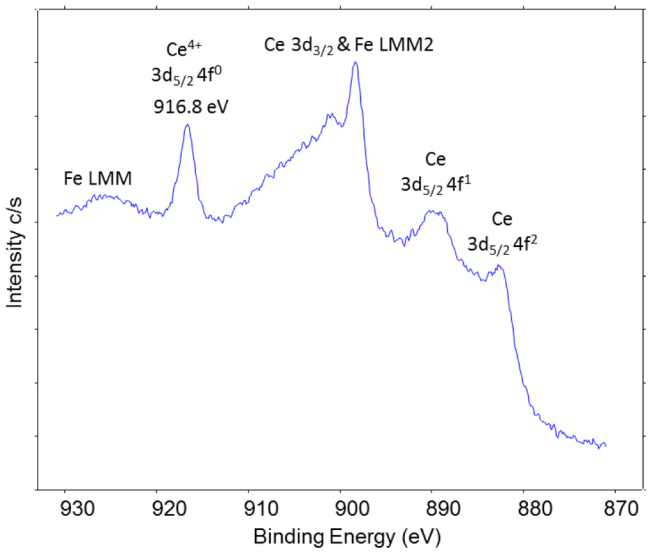

Figure 6. High-energy resolution photoemission spectra of the Ce 3d spectral region. The Ce $3d_{5/2}$ $4f^0$ line at 916.8 eV confirms the presence of significant Ce^{4+}.

the easy magnetization axis in tetrahedral and octahedral environments, respectively.[58] Substituted YIGs, on the other hand, display two tetrahedral sextets in accord with previous studies.[26,59] These two sextets are likely due to two distinct environments with different short-range ordering, as noted in $(Ca_{3-x}A_x)(Zr_{2-y}Fe_y)Fe_3O_{12}$ garnets, where A = Ce, Th, and Gd.[60] Substitution of cations in the *c* site also affected the octahedral Fe^{3+} environment to some extent.

The charge-coupled substitutions of Ca,Ce, and Ca,Th in YIG introduce systematic changes to the structure, especially to the tetrahedral Fe^{3+} sublattice. In both series, sextet peaks broadened roughly linearly with increasing *x* (Figure 7). Line broadening is due to gradual microscopic distortion of Fe^{3+} local environments of the *d* sublattice with increasing substitution of Ca^{2+},M^{4+} in the *c* site that generates multiple environments with similar parameters. A linear increase in *c*-site average cation size with *x* may cause such systematic line broadening. However, from the extent of line broadening with *x*, it appears that Ca^{2+},M^{4+} loading affects tetrahedral and octahedral sublattices very differently (Figure 7a and 7b). Relatively smaller changes in *a* and *a*′ line widths than in the tetrahedral line widths, however, suggest that Ca^{2+},M^{4+} cations in the *c* sites have a minor effect on the octahedral sublattice. Furthermore, the nature of the M^{4+} cation appears not to be critical since Ca^{2+},Ce^{4+}:YIG and Ca^{2+},Th^{4+}:YIG spectra have identical line widths for a given *x* (Figure 7).

Although the substitution only occurs in the *c* site in the YIG host (Ce:YIG,[26] Th:YIG,[27] La:YIG[59]), there are major differences in substitution and thermodynamic stability among Ca^{2+},M^{4+}:YIG garnets and single-substituted YIG garnets. For instance, it is clear that the YIG structure is more receptive to $Ca^{2+}-M^{4+}$ couple than to La^{3+} substitution. A 1.45 apfu of Y can be substituted by $Ca^{2+}-M^{4+}$ in Ca^{2+},M^{4+}:YIG $[(Y_{1.58}Ca_{0.71}Ce_{0.71})Fe_5O_{12}$ or $(Y_{1.55}Ca_{0.72}Th_{0.70}Fe_{0.03})Fe_5O_{12}]$, while only about one-half of that amount was achievable in La^{3+}:YIG $(Y_{2.2}La_{0.8}Fe_5O_{12})$. On the other hand, the highest concentration of Ce or Th in Ca^{2+},M^{4+}:YIG is 0.7 apfu, compared to only 0.2 apfu of Ce in Ce:YIG[26] and 0.07 apfu of Th in Th:YIG.[27] Thus, in general, these comparisons suggest that YIG structures have higher affinity toward the charge-coupled substitution of $Ca^{2+}-M^{4+}$ than for the substitution of large trivalent or tetravalent ions alone. Therefore, the charge-coupled substitution can better use the capacity of YIG as a host to incorporate more lanthanide and actinide ions.

$Y_{3-x}Ca_{0.5x}M_{0.5x}Fe_5O_{12}$ garnets are thermodynamically stable with respect to physical mixtures of their binary oxides as shown by the large negative values of $\Delta H_{f,ox}$. $\Delta H_{f,ox}$ of each substituted YIG was compared with that of undoped YIG for determining the thermodynamic stability of substitution based on the following reaction

$$Y_3Fe_5O_{12} + 0.5xCaO + 0.5xMO_2 \rightarrow Y_{3-x}Ca_{0.5x}M_{0.5x}Fe_5O_{12} + 0.5xY_2O_3\,(M = Ce, Th) \quad (1)$$

The enthalpies of substitution (ΔH_{sub}, Table 4) for reaction 1, calculated by subtracting $\Delta H_{f,ox}$ of the substituted YIG from that of undoped YIG, are positive and increase with the extent

Table 2. Enthalpies of Drop Solution and Enthalpies of Formation of $Y_{3-x}Ca_{0.5x}M_{0.5x}Fe_5O_{12}$ (M = Ce, Th) from Binary Oxides and from Elements at 25 °C

sample	Ce or Th amount 0.5*x*	ΔH_{ds}(kJ/mol)	$\Delta H_{f,ox}$(kJ/mol)[b]	ΔH°_f(kJ/mol)[c]
YIG	0	110.79 ± 1.76 (10)[26a]	−55.75 ± 3.24[26]	−4979.1 ± 5.7[26]
				−4979.0[52]
0.1Ca,0.1Ce:YIG	0.1	118.61 ± 1.2 (7)	−53.02 ± 2.95	−4958.3 ± 5.5
0.2Ca,0.2Ce:YIG	0.2	119.23 ± 0.9 (6)	−43.09 ± 2.79	−4930.2 ± 5.3
0.3Ca,0.3Ce:YIG	0.3	123.19 ± 0.8 (6)	−36.50 ± 2.76	−4905.5 ± 5.1
0.4Ca,0.4Ce:YIG	0.4	129.47 ± 1.6 (10)	−32.2. ± 3.11	−4883.1 ± 5.2
0.5Ca,0.5Ce:YIG	0.5	132.73 ± 3.04 (6)	−24.94 ± 4.07	−4857.6 ± 5.8
0.7Ca,0.7Ce:YIG	0.7	132.68 ± 1.64 (4)	−3.78 ± 3.26	−4800.2 ± 5.1
0.1Ca,0.1Th:YIG	0.1	111.51 ± 1.19 (5)	−53.37 ± 2.93	−4972.4 ± 5.5
0.2Ca,0.2Th:YIG	0.2	112.74 ± 1.38 (7)	−51.52 ± 2.99	−4966.2 ± 5.4
0.3Ca,0.3Th:YIG	0.3	106.78 ± 0.90 (6)	−42.46 ± 2.79	−4952.8 ± 5.2
0.4Ca,0.4Th:YIG	0.4	104.36 ± 0.33 (6)	−36.95 ± 2.66	−4942.9 ± 5.1
0.5Ca,0.5Th:YIG	0.5	94.90 ± 0.80 (5)	−24.43 ± 2.80	−4926.0 ± 5.2
0.7Ca,0.7Th:YIG	0.7	90.70 ± 1.00 (6)	−13.99 ± 2.90	−4897.2 ± 5.4

[a]Uncertainty is two standard deviations of the average value, number of measurements in parentheses. [b]Data taken from Table 3. [c]Data taken from Table S4, Supporting Information.

DOI: 10.1021/acs.inorgchem.5b00444
Inorg. Chem. 2015, 54, 4156−4166

Table 3. Thermochemical Cycles for Determination of the Enthalpies of Formation of Garnets from Binary Oxides (based on drop solution calorimetry in molten $3NaO{\cdot}4MoO_3$ at 702 °C)

reaction	ΔH (kJ/mol)
(1) $Y_{3-x}Ca_{0.5x}Ce_{0.5x}Fe_5O_{12(s,25\ °C)} \rightarrow (3-x)/2Y_2O_{3(sln,702\ °C)} + 5/2Fe_2O_{3(sln,702\ °C)} + 0.5xCaO_{(sln,702\ °C)} + 0.5xCeO_{2(sln,702\ °C)}$	$\Delta H_1 = \Delta H_{ds}$
(2) $Y_{3-x}Ca_{0.5x}Th_{0.5x}Fe_5O_{12(s,25\ °C)} \rightarrow (3-x)/2Y_2O_{3(sln,702\ °C)} + 5/2Fe_2O_{3(sln,702\ °C)} + 0.5xCaO_{(sln,702\ °C)} + 0.5xThO_{2(sln,702\ °C)}$	$\Delta H_2 = \Delta H_{ds}$
(3) $Y_2O_{3(s,25\ °C)} \rightarrow Y_2O_{3(sln,702\ °C)}$	$\Delta H_3 = -120.74 \pm 0.94$ (9)[53]
(4) $Fe_2O_{3(s,25\ °C)} \rightarrow Fe_2O_{3(sln,702\ °C)}$	$\Delta H_4 = 94.46 \pm 0.93$ (8)[54]
(5) $CaO_{(s,25\ °C)} \rightarrow CaO_{(sln,702\ °C)}$	$\Delta H_5 = -90.70 \pm 1.67$ (6)[55]
(6) $CeO_{2(s,25\ °C)} \rightarrow CeO_{2(sln,702\ °C)}$	$\Delta H_6 = 75.47 \pm 1.09$ (35)[56]
(7) $ThO_{2(s,25\ °C)} \rightarrow ThO_{2(sln,702\ °C)}$	$\Delta H_7 = 0.89 \pm 0.48$ (3)[56]
(8) $(3-x)/2Y_2O_{3(s,25\ °C)} + 5/2Fe_2O_{3(s,25\ °C)} + 0.5xCaO_{(s,25\ °C)} + 0.5xCeO_{2(s,25\ °C)} \rightarrow Y_{3-x}Ca_{0.5x}Ce0.5_xFe_5O_{12(s,25\ °C)}$, $\Delta H_{f,ox} = -\Delta H_1 + (3-x)/2\Delta H_3 + 5/2\Delta H_4 + 0.5x\Delta H_5 + 0.5x\Delta H_6$	$\Delta H_8 = \Delta H_{f,ox}$
(9) $(3-2x)/2Y_2O_{3(s,25\ °C)} + 5/2Fe_2O_{3(s,25\ °C)} + 0.5xCaO_{(s,25\ °C)} + 0.5xThO_{2(s,25\ °C)} \rightarrow Y_{3-x}Ca_{0.5x}Th_{0.5x}Fe_5O_{12(s,25\ °C)}$, $\Delta H_{f,ox} = -\Delta H_2 + (3-x)/2\Delta H_3 + 5/2\Delta H_4 + 0.5x\Delta H_5 + 0.5x\Delta H_7$	$\Delta H_9 = \Delta H_{f,ox}$

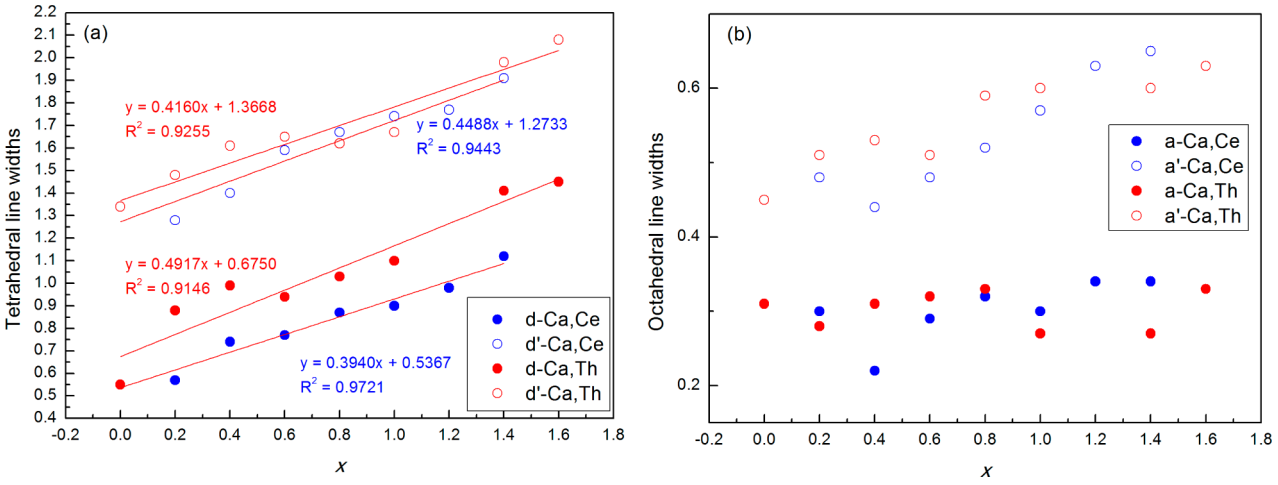

Figure 7. Charge-coupled substitutions introduce systematic broadening of sextet peaks: (a) line widths of tetrahedral Fe against x; (b) line widths of octahedral Fe against x.

Table 4. Enthalpies, Entropies, and Gibbs Free Energies of Substitution at 25 and 400 °C

sample	ΔH_{sub} (kJ/mol)	ΔS_{sub} (J/mol·K)	ΔG_{sub} (kJ/mol)	$\Delta G^{400\ °C}{}_{sub}$ (kJ/mol)
0.1Ca,0.1Ce:YIG	2.73 ± 2.16	7.26	0.57 ± 2.16	−2.9 ± 2.2
0.2Ca,0.2Ce:YIG	12.66 ± 2.00	12.10	9.05 ± 2.00	3.0 ± 2.0
0.3Ca,0.3Ce:YIG	19.25 ± 2.03	15.94	14.50 ± 2.03	6.2 ± 2.0
0.4Ca,0.4Ce:YIG	23.52 ± 2.54	19.08	17.84 ± 2.54	7.6 ± 2.5
0.5Ca,0.5Ce:YIG	30.82 ± 3.68	21.64	24.36 ± 3.68	12.3 ± 3.2
0.7Ca,0.7Ce:YIG	51.97 ± 2.86	25.30	44.42 ± 2.86	29.5 ± 2.9
0.1Ca,0.1Th:YIG	2.38 ± 2.13	7.26	0.21 ± 2.13	−3.9 ± 2.1
0.2Ca,0.2Th:YIG	4.23 ± 2.27	12.10	0.63 ± 2.27	−6.6 ± 2.3
0.3Ca,0.3Th:YIG	13.29 ± 2.06	15.94	8.53 ± 2.06	−1.5 ± 2.1
0.4Ca,0.4Th:YIG	18.80 ± 1.96	19.08	13.11 ± 1.96	0.5 ± 2.0
0.5Ca,0.5Th:YIG	31.36 ± 2.14	21.64	24.87 ± 2.14	10.0 ± 2.2
0.7Ca,0.7Th:YIG	41.74 ± 2.40	25.30	34.22 ± 2.40	15.2 ± 2.5

of substitution (Figure 8a and 8b). Diminishing the energetic stability for substituted garnet phases with higher Ce or Th content may be due to both the lattice expansion and the tetrahedral Fe sublattice distortions.

Compared to Ce:YIG, there is a great improvement in the energetic stability of Ca^{2+},M^{4+}:YIG. For 0.1 apfu of Ce, ΔH_{sub} of 0.1Ca,0.1Ce:YIG is 2.7 ± 2.2 kJ/mol which is much less endothermic than 12.7 ± 2.9 kJ/mol of 0.1Ce:YIG. For 0.2 apfu of Ce, ΔH_{sub} of 0.2Ca,0.2Ce:YIG is 12.7 ± 2.0 kJ/mol, which is also less destabilizing than the value of 26.4 ± 2.2 kJ/mol for 0.2Ce:YIG. Reduction reactions, such as $Ce^{4+} \rightarrow Ce^{3+}$ or $Fe^{3+} \rightarrow Fe^{2+}$, are thermodynamically unfavorable in air and could prevent further substitution in YIG.[26] Thus, because such reactions were avoided during the formation of Ca,M:YIG by introducing Ca^{2+}, Ce^{4+} couples with Ca^{2+} rather than with Fe or Ce reduction. As a result, ΔH_{sub} is significantly less positive and the extent of substitution is greatly increased.

Changes of entropy (ΔS_{sub}, Table 4) in reaction 1 originate from the structural changes of Ca,M:YIGs due to the substitution. Changes of thermal (vibrational) entropy are generally small for solid−solid reactions like reaction 1. As the result of cation mixing, the configurational entropy is

DOI: 10.1021/acs.inorgchem.5b00444
Inorg. Chem. 2015, 54, 4156−4166

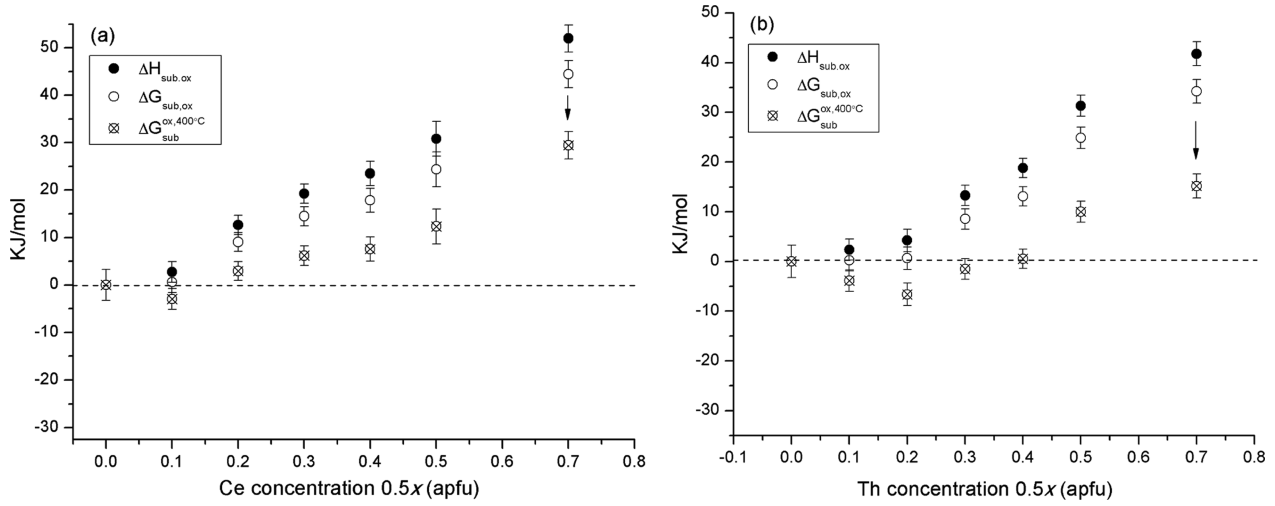

Figure 8. Enthalpies of substitution at room temperature (filled circles), Gibbs free energies of substitution at room temperature (open circles), and Gibbs free energies of substitution at 400 °C (cross-centered circles) of Ca,Ce:YIGs (a) and Ca,Th:YIGs (b). All plotted values are listed in Table 4.

considered the leading term for the overall ΔS_{sub}. This term rises from the (assumed) random distribution of introduced Ca^{2+} and M^{4+} and the remaining Y^{3+} in the dodecahedral sites. The Boltzmann entropy formula was used to calculate ΔS_{sub}

$$\begin{aligned}&\Delta S_{sub}(x\mathrm{Ca}^{2+}, \mathrm{M}^{4+}\text{: YIG})\\ &= S_{conf}(\mathrm{Ca}^{2+}, \mathrm{M}^{4+}, \mathrm{Y}^{3+})\\ &= -3R\left[\frac{3-x/2}{3}\ln\left(\frac{3-x/2}{3}\right)+\frac{x}{6}\ln\frac{x}{6}\right]-\frac{x}{2}R\ln\frac{1}{2}\end{aligned} \quad (2)$$

The entropy contribution, $-T\Delta S_{sub}$, plays an important role in enhancing the thermodynamic stability of Ca,M:YIG. The Gibbs free energies ($\Delta G_{sub} = \Delta H_{sub} - T\Delta S_{sub}$, Table 4, Figure 8) at room temperature are lower than ΔH_{sub} by 2.2−7.5 kJ/mol. As clearly seen in Figure 8a, Ca,Ce:YIG sample with a Ce content less than 0.1 apfu has near zero ΔG_{sub}, suggesting the substitution has only a slight impact on the stability of the YIG phase. For Ce content larger than 0.2 apfu, the enthalpy term increases in a much faster rate than the entropy term, such that $-T\Delta S_{sub}$ at room temperature can no longer compensate for the positive value of ΔH_{sub}. A similar trend was seen for Ca,Th:YIGs in Figure 8b. The Ca,Th substitution has almost a zero impact on the stability of YIG phase with Th content less than 0.2 apfu, which corresponds to 0.4 apfu of Y having been substituted. At Th content larger than 0.3 apfu, the enthalpy term begins to increase sharply to more endothermic values.

As temperature increases, the significance of $-T\Delta S_{sub}$ also rises. Consider T = 400 °C, which is within the temperature range of nuclear waste repositories storing spent nuclear fuel.[61,62] For Ca,Th:YIGs, see Figure 8b, the stability region for Th content in the system extends to 0.4 apfu, beyond which the free energies of substitution at 400 °C ($\Delta G^{400\ ^\circ C}_{sub}$, Table 4) are positive. Similarly, Ca,Ce:YIG extends its stability region to 0.3 apfu of Ce. Thus, we conclude that the high temperature in nuclear waste repositories favors stabilizing Ca,M:YIG garnets that contain moderate amounts of Ce or Th, which is consistent with the study on the Ce:YIG garnet host.[26]

At the synthesis temperature (1300 °C), the Gibbs free energy of substitution of Ca,M:YIGs with 0.7 apfu of Ce or Th content is almost zero and becomes positive at higher loading. This explains why it is difficult to produce a single-phase garnet with more than 0.7 apfu of Ce or Th at 1300 °C.

The pattern of thermodynamic stability shown by this study suggests that the charge balancing of tetravalent substitution by Ca, rather than by redox reactions with Ce or Fe, produces much more stable garnets and extends the accessible range of actinide loading in YIG-based garnets. It is likely that a similar conclusion holds for uranium substitution, and U^{4+}−Ca^{2+} substitution for trivalent ions in dodecahedral sites may be the best way to accommodate large loading of actinides in the garnet structure. However, the presence of higher uranium oxidation states may complicate the energetics. More complex garnet compositions may need to be tailored to provide stability with respect to other phases in a multiphase ceramic waste form and in the repository environment, but this study of a simple model system suggests a general mechanism for thermodynamically favorable actinide incorporation.

CONCLUSION

Significant amounts of Ce or Th were substituted into $Y_{3-x}Ca_{0.5x}M_{0.5x}Fe_5O_{12}$ (M = Ce, Th) garnet matrices. The structural changes due to the substitution, especially systematic distortions of tetrahedral Fe sites, were observed in Mössbauer spectroscopy. Even though the substitution occurs only in dodecahedral sites, it has significant and consistent influences on Fe in tetrahedral sites. The thermodynamic stability decreases with increasing Ce or Th content but is improved at higher temperature due to the entropic contribution. The knowledge of structures and thermodynamic properties of $Y_{3-x}Ca_{0.5x}M_{0.5x}Fe_5O_{12}$ suggests a possible favorable substitution mechanism for the application of this garnet host or other similar hosts for immobilizing lanthanides/actinides under repository conditions.

ASSOCIATED CONTENT

Supporting Information

PXRD patterns and completed Mössbauer spectra, tabulated EPMA chemical analysis, tabulated Mössbauer spectral parameters for $Y_{3-x}Ca_{0.5x}Th_{0.5x}Fe_5O_{12}$, and thermochemical cycles for garnet from elements at 25 °C. This material is available free of charge via the Internet at http://pubs.acs.org.

DOI: 10.1021/acs.inorgchem.5b00444
Inorg. Chem. 2015, 54, 4156−4166

AUTHOR INFORMATION

Corresponding Author

*E-mail: anavrotsky@ucdavis.edu.

Notes

The authors declare no competing financial interest.

ACKNOWLEDGMENTS

The authors thank Dr. Amir H. Tavakoli for helping with experiments and valuable discussion of thermodynamic data. This material is based upon work supported as part of the Materials Science of Actinides, an Energy Frontier Research Center funded by the U.S. Department of Energy, Office of Science, Office of Basic Energy Sciences under Award Number DESC0001089. Mössbauer spectroscopic and XPS analysis were performed at the Environmental Molecular Sciences Laboratory (EMSL), a national scientific user facility sponsored by the DOE's Office of Biological and Environmental Research and is located at Pacific Northwest National Laboratory (PNNL). PNNL is operated by Battelle for the U.S. DOE under contract DE-AC06-76RLO1930. Portions of this work were performed at GeoSoilEnviroCARS (Sector 13), Advanced Photon Source (APS), Argonne National Laboratory. GeoSoilEnviroCARS is supported by the National Science Foundation-Earth Sciences (EAR-1128799) and Department of Energy-GeoSciences (DE-FG02-94ER14466). Use of the Advanced Photon Source was supported by the U.S. Department of Energy, Office of Science, Office of Basic Energy Sciences, under Contract No. DE-AC02-06CH11357. We also gratefully acknowledge the support of the U.S. Department of Energy through the LANL/LDRD Program and the G. T. Seaborg Institute for this work.

REFERENCES

(1) Lutze, W.; Ewing, R. C. *Radioactive Waste Forms for the Future*; Elsevier: Amsterdam, 1988.

(2) Ewing, R. C. *Proc. Natl. Acad. Sci. U.S.A.* **1999**, *96*, 3432−3439.

(3) Ewing, R. C. *Elements* **2006**, *2*, 331−334.

(4) Laverov, N. P.; Velichkin, V. I.; Omel'yanenko, B. I.; et al. *Isolation of Spent Nuclear Materials: Geological and Geochemical Aspects*; IFZ RAN: Moscow, 2008.

(5) Weber, W. J.; Navrotsky, A.; Stefanovsky, S.; Vance, E. R.; Vernaz, E. *MRS Bull.* **2009**, *34*, 46−53.

(6) Sinclair, W.; Ringwood, A. E. *Geochem. J.* **1981**, *15*, 229−243.

(7) Ringwood, T. *Am. Sci.* **1982**, *70*, 201−207.

(8) Kesson, S. E.; Ringwood, A. E. *Radioact. Waste Manage.* **1983**, *4*, 159−174.

(9) Weber, W. J.; Ewing, R. C.; Angell, C. A.; Arnold, G. W.; Cormack, A. N.; Delaye, J. M.; Griscom, D. L.; Hobbs, L. W.; Navrotsky, A.; Price, D. L.; Stoneham, A. M.; Weinberg, W. C. *J. Mater. Res.* **1997**, *12*, 1946−1978.

(10) Burakov, B. E.; Anderson, E. B.; Knecht, D. A.; Zamoryanskaya, M. A.; Strykanova, E. E.; Yagovkina, M. A. *Mater. Res. Soc. Symp. Proc.* **1999**, *556*, 6.

(11) Yudintsev, S. V.; Lapina, M. I.; Ptashkin, A. G.; Ioudintseva, T. S.; Utsunomiya, S.; Wang, L. M.; Ewing, R. C. *Mater. Res. Soc. Symp. Proc.* **2002**, *713*, 477−480.

(12) Ewing, R. C.; Weber, W. J.; Lian, J. *J. Appl. Phys.* **2004**, *95*, 5949−5971.

(13) Urusov, V. S.; Organova, N. I.; Karimova, O. V.; Yudintsev, S. V.; Stefanovskii, S. V. *Dokl. Earth Sci.* **2005**, *401*, 319−325.

(14) Rusakov, V. S.; Urusov, V. S.; Kovalchuk, R. V.; Kabalov, Y. K.; Yudincev, S. V. *Hyperfine Interact.* **2005**, *164*, 99−104.

(15) Utsunomiya, S.; Yudintsev, S.; Ewing, R. C. *J. Nucl. Mater.* **2005**, *336*, 251−260.

(16) Lumpkin, G. R. *Elements* **2006**, *2*, 365−372.

(17) Yudintsev, S. V.; Stefanovsky, S. V.; Ewing, R. C. Actinide host phases as radioactive waste forms. In *Structural Chemistry of Inorganic Actinide Compounds*; Krivovichev, S., Burns, P., Tananaev, I. G., Eds.; Elsevier: Amsterdam, 2007; pp 457−490.

(18) Omel'yanenko, B. I.; Livshits, T. S.; Yudintsev, S. V.; Nikonov, B. S. *Geol. Ore Deposit* **2007**, *49*, 173−193.

(19) Galuskina, I. O.; Galuskin, E. V.; Armbruster, T.; Lazic, B.; Kusz, J.; Dzierzanowski, P.; Gazeev, V. M.; Pertsev, N. N.; Prusik, K.; Zadov, A. E.; Winiarski, A.; Wrzalik, R.; Gurbanov, A. G. *Am. Mineral.* **2010**, *95*, 1172−1181.

(20) Utsunomiya, S.; Wang, L. M.; Ewing, R. C. *Nucl. Instrum. Methods Phys. Res., Sect. B* **2002**, *191*, 600−605.

(21) Utsunomiya, S.; Wang, L. M.; Yudintsev, S.; Ewing, R. C. *J. Nucl. Mater.* **2002**, *303*, 177−187.

(22) Zhang, J. M.; Livshits, T. S.; Lizin, A. A.; Hu, Q. N.; Ewing, R. C. *J. Nucl. Mater.* **2010**, *407*, 137−142.

(23) Laverov, N. P.; Yudintsev, S. V.; Livshits, T. S.; Stefanovsky, S. V.; Lukinykh, A. N.; Ewing, R. C. *Geochem. Int.* **2010**, *48*, 1−14.

(24) Livshits, T. S. *Geol. Ore Deposits* **2008**, *50*, 470−481.

(25) Miro, P.; Pierrefixe, S.; Gicquel, M.; Gil, A.; Bo, C. *J. Am. Chem. Soc.* **2010**, *132*, 17787−94.

(26) Guo, X. F.; Tavakoli, A. H.; Sutton, S.; Kukkadapu, R. K.; Qi, L.; Lanzirotti, A.; Newville, M.; Asta, M.; Navrotsky, A. *Chem. Mater.* **2014**, *26*, 1133−1143.

(27) Guo, X. F.; Rak, Z.; Tavakoli, A. H.; Becker, U.; Ewing, R. C.; Navrotsky, A. *J. Mater. Chem. A* **2014**, *2*, 16945−16954.

(28) Gibbs, G. V.; Smith, J. V. *Am. Mineral.* **1965**, *50*, 2023−2039.

(29) Geller, S. *Z. Kristallogr. Kristallgeom. Kristallphys. Kristallchem.* **1967**, *125*, 4−5.

(30) Novak, G. A.; Gibbs, G. V. *Am. Mineral.* **1971**, *56*, 791−825.

(31) Donnerberg, H. *Springer Tracts Mod. Phys.* **1999**, *151*, 165−190.

(32) Whittle, K. R.; Lumpkin, G. R.; Berry, F. J.; Oates, G.; Smith, K. L.; Yudintsev, S.; Zaluzec, N. J. *J. Solid State Chem.* **2007**, *180*, 785−791.

(33) Yudintsev, S. V. *Geol. Ore Deposits* **2003**, *45*, 151−165.

(34) Rak, Z.; Ewing, R. C.; Becker, U. *Phys. Rev. B* **2011**, *84*, 155128/1−155128/10.

(35) Rak, Z.; Ewing, R. C.; Becker, U. *J. Phys.: Condens. Matter* **2013**, *25*, 495502.

(36) Gramsch, S. A.; Morss, L. R. *J. Alloys Compd.* **1994**, *207*, 432−435.

(37) Guo, X. Z.; Ravi, B. G.; Devi, P. S.; Hanson, J. C.; Margolies, J.; Gambino, R. J.; Parise, J. B.; Sampath, S. *J. Magn. Magn. Mater.* **2005**, *295*, 145−154.

(38) Vajargah, S. H.; Hosseini, H. R. M.; Nemati, Z. A. *J. Alloys Compd.* **2007**, *430*, 339−343.

(39) Rancourt, D. G.; Ping, J. Y. *Nucl. Instrum. Methods Phys. Res., Sect. B* **1991**, *58*, 85−97.

(40) Peretyazhko, T. S.; Zachara, J. M.; Kukkadapu, R. K.; Heald, S. M.; Kutnyakov, I. V.; Resch, C. T.; Arey, B. W.; Wang, C. M.; Kovarik, L.; Phillips, J. L.; Moore, D. A. *Geochim. Cosmochim. Acta* **2012**, *92*, 48−66.

(41) Sutton, S. R.; Bertsch, P. M.; Newville, M.; Rivers, M.; Lanzirotti, A.; Eng, P. *Rev. Mineral. Geochem.* **2002**, *49*, 429−483.

(42) Haskel, D. FLUO: correcting XANES for self absorption in fluorescence measurements. http://www.aps.anl.gov/xfd/people/haskel/fluo.html.

(43) Kraft, S.; Stumpel, J.; Becker, P.; Kuetgens, U. *Rev. Sci. Instrum.* **1996**, *67*, 681−687.

(44) Ravel, B.; Newville, M. *J. Synchrotron Radiat.* **2005**, *12*, 537−541.

(45) Navrotsky, A. *Phys. Chem. Mineral.* **1977**, *2*, 89−104.

(46) Navrotsky, A. *Phys. Chem. Mineral.* **1997**, *24*, 222−241.

(47) Navrotsky, A.; Rapp, R. P.; Smelik, E.; Burnley, P.; Circone, S.; Chai, L.; Bose, K. *Am. Mineral.* **1994**, *79*, 1099−1109.

(48) Navrotsky, A. *J. Am. Ceram. Soc.* **2014**, *97*, 3349−3359.

(49) Zhang, J.; Wu, Z. Y.; Liu, T.; Hu, T. D.; Wu, Z. H.; Ju, X. *J. Synchrotron Radiat.* **2001**, *8*, 531−532.

DOI: 10.1021/acs.inorgchem.5b00444
Inorg. Chem. 2015, 54, 4156−4166

(50) Shahin, A. M.; Grandjean, F.; Long, G. J.; Schuman, T. P. *Chem. Mater.* **2005**, *17*, 315−321.
(51) Henderson, M. A.; Perkins, C. L.; Engelhard, M. H.; Thevuthasan, S.; Peden, C. H. F. *Surf. Sci.* **2003**, *526*, 1−18.
(52) Pankratz, L. B. *Thermodynamic Properties of Carbides, Nitrides, and Other Selected Substances*; U.S. Dept. of the Interior, Bureau of Mines: Washington, DC, 1994.
(53) Chen, W. Q.; Lee, T. A.; Navrotsky, A. *J. Mater. Res.* **2005**, *20*, 144−150.
(54) Lilova, K. I.; Xu, F.; Rosso, K. M.; Pearce, C. I.; Kamali, S.; Navrotsky, A. *Am. Mineral.* **2012**, *97*, 164−175.
(55) Helean, K. B.; Navrotsky, A.; Vance, E. R.; Carter, M. L.; Ebbinghaus, B.; Krikorian, O.; Lian, J.; Wang, L. M.; Catalano, J. G. *J. Nucl. Mater.* **2002**, *303*, 226−239.
(56) Helean, K. B.; Navrotsky, A.; Lumpkin, G. R.; Colella, M.; Lian, J.; Ewing, R. C.; Ebbinghaus, B.; Catalano, J. G. *J. Nucl. Mater.* **2003**, *320*, 231−244.
(57) Sawatzky, G. A.; Vanderwo, F.; Morrish, A. H. *Phys. Rev.* **1969**, *183*, 383−386.
(58) Lyubutin, I. S.; Gavriliuk, A. G.; Trojan, I. A.; Sadykov, R. A. *JETP Lett.* **2005**, *82*, 702−707.
(59) Cheng, Z. J.; Cui, Y. M.; Yang, H.; Chen, Y. *J. Nanopart. Res.* **2009**, *11*, 1185−1192.
(60) Urusov, V. S.; Rusakov, V. S.; Kabalov, Y. K.; Yudintsev, S. V. *Dokl. Phys.* **2004**, *49*, 715−722.
(61) Wigeland, R. A.; Bauer, T. H.; Fanning, T. H.; Morris, E. E. *Nucl. Technol.* **2006**, *154*, 95−106.
(62) Bodansky, D. *Nuclear energy: Principles, practices, and prospects*; American Institute of Physics: Woodbury, NY, 1996; pp 246−273.

DOI: 10.1021/acs.inorgchem.5b00444
Inorg. Chem. 2015, 54, 4156−4166